Biochemistry

pubs.acs.org/biochemistry Article

Phage-Related Ribosomal Protease (Prp) of *Staphylococcus aureus*: In Vitro Michaelis–Menten Kinetics, Screening for Inhibitors, and Crystal Structure of a Covalent Inhibition Product Complex

Julia A. Hotinger, Heather A. Pendergrass, Darrell Peterson, H. Tonie Wright, and Aaron E. May*

Cite This: *Biochemistry* 2022, 61, 1323–1336 Read Online

ACCESS | Metrics & More | Article Recommendations | Supporting Information

ABSTRACT: Phage-related ribosomal proteases (Prps) are essential for the assembly and maturation of the ribosome in Firmicutes, including the human pathogens *Staphylococcus aureus*, *Streptococcus pneumoniae*, and *Clostridium difficile*. These bacterial proteases cleave off an N-terminal extension of a precursor of ribosomal protein L27, a processing step that is essential for the formation of functional ribosomes. This essential role of Prp in these pathogens has identified this protease as a potential antibiotic target. In this work, we determine the X-ray crystal structure of a covalent inhibition complex at 2.35 Å resolution, giving the first complete picture of the active site of a functional Prp. We also characterize the kinetic activity and screen for potential inhibitors of Prp. This work gives the most complete characterization of the structure and specificity of this novel class of proteases to date.

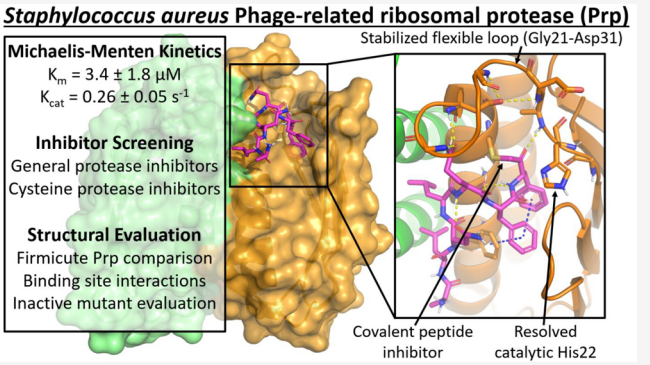

Antibiotic resistance is a global threat to human health. The past three decades have seen a decline in the number of new antibiotic approvals and an increase in the number of antibiotic-resistant pathogens.[1] The Centers for Disease Control and Prevention (CDC) estimate >2.8 million cases per year of antibiotic-resistant infections in the United States, a 40% increase from 6 years ago.[2] Approximately 10,600 deaths are attributable to methicillin-resistant *Staphylococcus aureus* (MRSA), a Gram-positive bacterial pathogen responsible for skin infections, pneumonia, and sepsis. Since 2006, contractions of MRSA have been monitored by the National and State Healthcare-Associated Infections Report through the CDC.[3] Over the first decade of monitoring, the rate of hospital-acquired MRSA infections decreased due to the vigilant implementation of protocols designed to improve patients' protection from infection. These efforts notwithstanding, the overall rate of MRSA infection remains high, with more than 323,000 cases reported in 2017.[2] There is an urgent need for new antibiotics, new antibiotic targets, and antibacterial agents that have a limited ability to harm commensal bacteria. One such strategy is to employ narrow-spectrum antibiotics that are more selective for their pathogenic targets.[4−7]

The Christie lab identified and functionally characterized phage-related ribosomal protease (Prp) from *S. aureus*, which is responsible for the essential post-translational cleavage of a supernumerary N-terminal extension of a precursor ribosomal protein L27.[8] This novel cysteine protease was initially discovered while studying the capsid assembly of staphylococcal phage 80*α*. Some phages encode a protease to cleave their structural proteins during maturation (e.g., a scaffold removed from the capsid protein after assembly).[9] 80*α*, however, does not encode such a protease, implying cleavage of major capsid and scaffold proteins gp46 and gp47 is dependent on staphylococcal host proteases for phage maturation. This is supported by the cleavage observed after gp46 and gp47 are expressed in *S. aureus* but not observed upon their expression in *Escherichia coli*. The aforementioned novel cysteine protease, later called Prp, was found to be this protease for 80*α* capsid proteins gp46 and gp47.[8]

To identify Prp's endogenous ligand in *S. aureus*, a blast search of the cleavage sites of 80*α* capsid proteins gp46 and gp47 against the *S. aureus* proteome was performed. This search revealed that *S. aureus* ribosomal protein L27 is synthesized as a precursor (pre-L27) with an N-terminal cleavage sequence similar to those of 80*α* proteins gp46 and gp47 (Table 1). L27 is necessary for ribosomal maturation and plays an essential role in stabilizing the 3′ end of tRNA during protein synthesis.[10] The interaction between Prp and pre-L27 with cleavage of the N-terminal sequence of pre-L27 is

Received: January 7, 2022
Revised: June 7, 2022
Published: June 22, 2022

Table 1. Amino Acid Sequence Alignment of Staphylococcal Phage 80α Proteins with L27 of *S. aureus* and *E. coli*

Name	Sequence
80α Scaffold (gp46)	ME-ENKLKFNLQFF′ADQSDDPDEPGGDGK...
80α Capsid (gp47)	MEQTQKLKLNLQHF′ASNNVKPQVFNPDNV...
S. aureus L27	-----MLKLNLQFF′ASKKGVSSTKNGRDS...
E. coli L27	----------M′AHKKAGGSTRNGRDS...

High conservation to 80α, moderate conservation to 80α, High conservation to *E. coli* L27, moderate conservation to *E. coli* L27. Alignments were performed with Cluster Omega. Accession numbers: gp46, A4ZFB2; gp47, A4ZBF3; *Sa*L27, Q2FXT0; *Ec*L27, P0A7L8.

Table 2. L27 N-Terminal Amino Acid Sequences of Prp-Containing Bacteria

Phylum	Species	L27 N-terminus
Firmicutes	*Bacillus subtilis*	MLRL---DLQFF′ASKK...
	Clostridioides difficile †	MLNM---NLQLL′ASKK...
	Enterococcus faecium	MLLSM--NLQLF′AHKK...
	Lactobacillus rhamnosus	MLKM---NLQFF′SHHK...
	Staphylococcus aureus †	MLKL---NLQFF′ASKK...
	Streptococcus mutans †	MLKMNLANLQLF′AHKK...
	Streptococcus pneumoniae †	M---TLNNLQLF′AHKK...
Fusobacteria	*Fusobacterium nucleatum*	M--QFLFNIQLF′AHKK...
Synergistetes	*Aminobacterium colombiense*	M-RINFFDLQFF′AHKK...
Spirochetes	*Borrelia burgdorferi* †	M----------′ATSK...
Tenericutes	*Mycoplasma pneumonia* †	M----------′ASKK...
Thermotogae	*Thermotoga maritima*	M----------′AHKK...

†Obligate pathogen, high conservation, moderate conservation. Alignments were performed with Cluster Omega.

essential for ribosomal maturation in *S. aureus* and in other Firmicute bacteria that contain L27 with an N-terminal extension (termed long L27).[8] *S. aureus* L27 knockouts are nonviable in the presence of "precleaved" L27 that lacks the N-terminal peptide extension or in the presence of "uncleavable" L27 mutants.[11] This indicates that the cleavage process performed by Prp is necessary for cell survival, suggesting that Prp could be a novel target for antibiotics.

After the cleavage function of Prp was determined in *S. aureus* by Wall et al.,[11] *Sa*Prp became the prototype member of family C.108 (cysteine proteases, group number 108) and clan CR.[8] [An earlier Prp from *Thermotoga maritima* had been isolated and crystallized and shown to have a novel fold pattern (from N → C, *ββαβαβ*), but its function had yet to be determined at that time.[12]] There are no human homologues of family C.108 or clan CR, and there is currently only one other member of clan CR, a cysteine protease responsible for cleaving an ∼40-amino acid N-terminal extension from a capsid protein in staphylococcal bacteriophage CP-1.[13]

Prp is knockout lethal in *S. aureus*, and expression of precleaved L27 in *S. aureus* results in severe growth defects.[8] This is consistent with Prp having a chaperone function toward L27 for ribosomal assembly before or after cleaving the N-terminal sequence. It is noteworthy that genes for L27 and Prp, *rpmA* and *ysxB*, respectively, are directly next to each other on the genome, much like other ribosomal protein−chaperone pairs.[14] Both *rpmA* and *ysxB* have been classified as essential in *S. aureus* by multiple methods.[15−17] This reiterates the potential of Prp as an antibiotic target.

Due to its recent discovery, Prp has never been explored as a drug target, meaning that resistance to Prp inhibitors is unlikely to have already developed. Bioinformatic analysis has shown that long L27 is present in Firmicutes, Fusobacteria, Synergistetes, and some Thermotogae and Tenericutes.[17,18] The L27 N-terminal extension is cleaved by its corresponding Prp and generally follows an MLxx(D/N)LQ(F/L)F′A(S/H)KK motif, where xx indicates a variable sequence (Table 2). All bacteria encoding long L27 also encode Prp.[17] Of the more than 40 formally recognized phyla of bacteria, only six were seen in our bioinformatic analysis to encode Prp. Any Prp inhibitor should be selective for this subset of bacteria, resulting in less selective pressure across bacteria as a whole.[8] This selective/narrow-spectrum target population should slow the rate of acquisition of resistance and cause fewer side effects from killing commensal bacteria. Additionally, pathogens such as *S. aureus*, *Streptococcus pneumoniae*, and *Clostridioides difficile* should be susceptible to Prp inhibition, regardless of their drug-resistance status against current antibiotics.

The general specificity of Prp has been documented, but the degree of selectivity between the Prps of pathogenic and commensal Firmicutes has yet to be established.[8,11,17,19,20] This is partly due to very limited in vitro data on the properties of the Prps and to a paucity of crystal structures for them and their complexes. To date, there are only four Prps with published crystal structures [*S. aureus*, Protein Data Bank (PDB) entry 4PEO; *Streptococcus mutans*, PDB entry 2G0I; *S. pneumoniae*, PDB entry 2IDL; and *T. maritima*, PDB entry 1S1L], all of which are not in the correct conformation for catalysis.[12,21−23] None of the three Firmicute Prp structures

https://doi.org/10.1021/acs.biochem.2c00010
Biochemistry 2022, 61, 1323−1336

(PDB entries 4PEO, 2G0I, and 2IDL) is of a commensal bacterium (*T. maritima* is considered commensal but is not a Firmicute and does not encode long L27). An improvement in understanding the differences between commensal and pathogenic Prps will help determine if it is possible to develop selective inhibitors for pathogens.

This work provides the first completely resolved structure of the functional active site of any Prp. The stabilization of the active site of *Sa*Prp was enabled by reaction with a pre-L27 mimic peptidyl-chloroketone suicide inhibitor, leading to a covalent complex that could be crystallized. In vitro analysis of the activity of the *Sa*Prp showed it to be resistant to a large panel of conventional protease inhibitors, emphasizing the uniqueness of the C.108 cysteine protease family. These and other findings will be useful for future inhibitor design against this therapeutic target.

MATERIALS AND METHODS

Materials. The peptide substrate (FITC-KLNLQFFASKK-Dnp) used for in vitro assays consisted of the *S. aureus* L27 cleavage sequence motif flanked by fluorophore fluorescein isothiocyanate (FITC) on the N-terminus and the quencher dinitrophenyl (Dnp) on the C-terminus (Figure 1, **1**). A peptide inhibitor substrate is used in crystallographic studies, acetyl-KLNLQFF-chloromethylketone (>95%, Ac-KLNLQFF-CMK). Both peptide substrates were purchased from United Biosystems (Herndon, VA). Screening compounds, including a 77-compound library of protease inhibitors, were purchased from Selleck Chemicals (Houston, TX). Mersalyl acid was acquired from Bios Laboratories, Inc. (New Haven, CT).

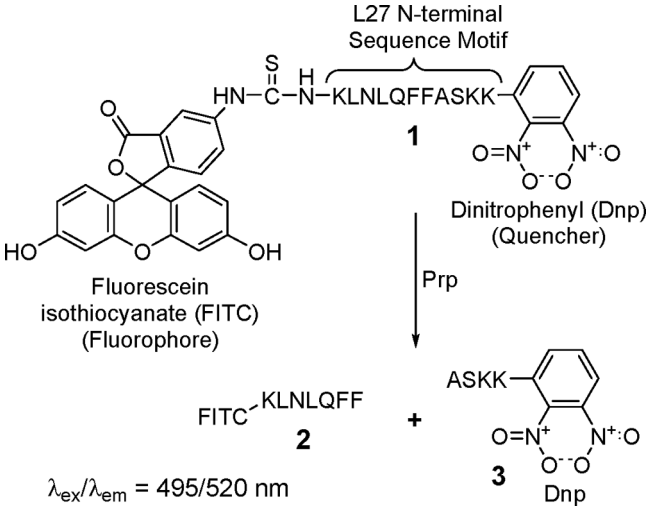

Figure 1. Prp cleaves the L27 mimic 11-mer peptide flanked by the fluorophore FITC and the quencher Dnp (**1**). Upon cleavage, the quencher (**3**) is released and the fluorescence of the fluorophore (**2**) is measured at 520 nm upon excitation at 495 nm.

Prp Expression and Purification. The native *S. aureus* Prp gene was cloned as a His6-SUMO N-terminal fusion protein from plasmid pEW34. In later work (see below), an N → Q mutation was introduced at residue 63 to obviate the possibility of deamidation at this site. The His6-SUMO-tagged Prp and His6-tagged ubiquitin-like protein-specific protease 1 (Ulp1) were overexpressed in BL21-CodonPlus (DE3)-RIL (Agilent Technologies, Santa Clara, CA) and ScarabXpress T7 lac (Scarab Genomics, Madison, WI) *E. coli* cells, respectively. Bacteria were lysed using an Emulsiflex C3 High-Pressure Homogenizer (Avestin Inc., Ottawa, ON) at approximately 20,000 psi. The lysate was clarified by centrifugation at 20,000 rpm for 30 min at 10 °C. A nickel affinity column was prepared by adding 10−20 mL of Profinity IMAC Uncharged Resin (Bio-Rad, Hercules, CA), followed by 5−10 mL of 100 mM nickel sulfate ($NiSO_4$). The column was washed with ∼30 mL of wash buffer [25 mM Tris (pH 8), 300 mM NaCl, and 10 mM imidazole], and the clarified supernatant was added to the column, allowing the His6-tagged protein to bind the resin. The bound protein was washed and eluted with ∼100 mL of elution buffer [25 mM Tris (pH 8), 300 mM NaCl, and 110 mM imidazole].

Fractions were analyzed by SDS−PAGE, and pooled fractions containing the protein of interest were concentrated and run on an S100 column (Sigma-Aldrich Co. LLC, St. Louis, MO) in 50 mM sodium phosphate buffer (pH 7.5) with 0.02% (v/v) sodium azide [and 10% (v/v) glycerol for Ulp1]. His6-tagged Ulp1 was added in an approximately 1:1 ratio by weight to His6-SUMO-Prp in 150 mM NaCl at room temperature, and 5 μL samples were taken at 0, 1, 2, and 3 h and analyzed for the extent of cleavage via SDS−PAGE. After sufficient cleavage, the mixture was dialyzed in 50 mM sodium phosphate buffer and 0.3 M NaCl and made 1 mM in dithiothreitol (DTT) before being run on a second nickel-TED affinity column (Macherey & Nagel) and the flow-through collected. The flow-through was spin concentrated to 1.2 mg/mL for the preparation of the inhibitor complex (below) and stored in 10% glycerol at −80 °C.

Later purification of *Sa*Prp for in vitro assays was performed as described above on the N63 → Q mutant, but with added steps. Pooled fractions from the second nickel column in 10 mM Tris (pH 7.5) were applied to a Bio-Rad Macroporous Q column equilibrated with 50 mM piperazine buffer (pH 5.3) and washed exhaustively until no absorbance was measured in the effluent. *Sa*Prp was then eluted as a single peak with a linear gradient from 0 to 1.0 M NaCl in piperazine buffer. The pooled peak fractions were immediately applied to a BioGel P6DG desalting column in 10 mM 4-(2-hydroxyethyl)-1-piperazineethanesulfonic acid (HEPES) buffer (pH 7.5) and 0.1 M NaCl, and the excluded volume *Sa*Prp peak made 10% in glycerol and stored in 1 mL aliquots at 0.5−1.0 mg/mL at −80 °C. Cloning, expression, and purification of the *C. difficile* Prp were performed as they were for *Sa*Prp through the second nickel column, but with some variation in the final purification steps (which will be described in the future).

Preparation and Crystallization of the SaPrp:Ac-KLNLQFF-CMK Covalent Complex. A thawed aliquot of 500 μL of *Sa*Prp in 50 mM sodium phosphate (pH 8.0) and 0.3 M NaCl was made 0.3 mM in tris(2-carboxyethyl)-phosphine (TCEP) and combined with 50 μL of dimethyl sulfoxide (DMSO) in which solid Ac-KLNLQFF-CMK at a final 2.6-fold molar excess over *Sa*Prp was dissolved. The clear solution was incubated for 1 h at room temperature, dialyzed against 10 mM HEPES (pH 7.5) and 0.25 M NaCl, and stored in 10% glycerol at −80 °C. Mass spectrometry confirmed the almost stoichiometric formation of the covalent complex (MW = 12,816 Da; >95%).

The thawed sample of Ac-KLNLQFF-CMK in complex with *Sa*Prp (henceforth described as Ac-KLNLQFF-CH_2- when covalently bound after reaction) was diluted with 10 mM HEPES (pH 7.5) to 0.1 M NaCl, TCEP added to a final concentration of 0.3 mM, 0.5 M Tris base (pH 7.5) added to a

https://doi.org/10.1021/acs.biochem.2c00010
Biochemistry 2022, 61, 1323−1336

final concentration of 3.3 mM, and the sample concentrated in Millipore cellulose spin concentrators to 50 μL. β-Octyl glucoside was then added to a final concentration of 0.5% (w/v). Hanging and sitting (2−3 μL) drops of equal volumes of fresh protein and reservoir precipitant from commercial screens were placed in Hampton vapor diffusion plates. Conditions in which crystals grew were refined, and crystals were grown for 92 days from drops with a reservoir precipitant of 28% Peg400, 0.2 M $CaCl_2$, and 0.1 M HEPES (pH 7.5).

Crystallographic Data Collection and Structure Determination. A crystal, cryoprotected briefly in a reservoir solution, was mounted in a liquid nitrogen vapor stream, and intensity data were collected on an in house Rigaku diffractometer with a Pilatus 200K hybrid pixel array detector, a high-brilliance rotating anode X-ray generator (MicroMax-007HF), VariMax-HF Arc-Sec optics, an AFC11 goniometer, and a Cryostream 800 cooler. A full sphere of intensity data to 2.2 Å resolution was processed using CrysAlis^{Pro} (Rigaku Corp., Oxfordshire, England), indexed in space group *I*2 with Pointless,[24] and scaled with Aimless[25] in CCP4.[26] A molecular replacement solution using the earlier structure of unliganded *Sa*Prp (PDB entry 4PEO) was obtained with Phaser[27] in Phenix.[28] Rigid body refinement of the model was followed by maximum likelihood parameter refinement in Phenix Refine[29] with recursive rebuilding and solvent addition in Coot.[30] Table S1 summarizes the data collection and refinement statistics. This structure was deposited as PDB entry 7KLD.

Fluorogenic Cleavage Assay. We optimized and miniaturized a Prp fluorogenic cleavage assay previously reported by the Christie lab.[11] The substrate for our assay was the *Sa*L27 cleavage sequence motif (KLNLQFFASKK) flanked with FITC as a fluorophore on the N-terminus and the quencher Dnp on the C-terminus [**1** (Figure 1)]. The peptide substrate was reconstituted in DMSO to 1 mM, and its concentration was determined by measuring the absorbance at 325 nm at a 0.1 cm path length with a BioTek Synergy HTX plate reader. Aliquots (20 μL) were stored at −20 °C until they were used. The assays (unless otherwise defined) were performed with purified N63 → Q mutant *Sa*Prp, produced as previously described. The concentration of Prp was checked via a standard Bradford assay.[31] The final assay concentration of Prp was 21.4 nM (calculated as a dimer) and 500 nM (FITC) peptide substrate.[11] Assays were performed in sodium phosphate buffer (50 mM, pH 7) with 1.5 mM DTT, 2.35 mM ethylenediaminetetraacetic acid (EDTA), and 0.01% Tween 20.

Assay buffer was dispensed into 1536-well plates (Fisherbrand 1536-well black flat-bottom) with the Multidrop Combi nL Reagent Dispenser (to a total volume of 5 μL) before the addition of Prp using a Labcyte Echo550 acoustic liquid handler. This solution was then shaken for at least 1 min on the Multidrop Combi nL Reagent Dispenser to ensure homogeneity. Compounds being screened were then added to final concentrations of 10−100 μM with a Labcyte Echo550 acoustic liquid handler before incubation at room temperature for 10 min. The peptide substrate was added to a final concentration of 0.5 μM immediately before monitoring fluorescence with a BMG Labtech CLARIOstar Plus plate reader. When Prp cleaved the peptide (**1**), the quencher (**3**) and FITC-peptide product (**2**) were released. The concentration of FITC from the intensity of the fluorescent signal was monitored for 45 min [λ_{ex} = 488 nm (15 nm), and λ_{em} = 530 nm (15 nm); gain of 2400]. Assay data were analyzed using Microsoft Excel for Microsoft 365. The percent inhibition of each compound was calculated from the initial rate of change in fluorescence compared to an uninhibited control using eq 1:

$$\%\ \text{inhibition} = 100\left(1 - \frac{m_C}{m_V}\right) \quad (1)$$

where *m* is the slope, C is the compound, and V is the vehicle.

Determining the *Z* Factor. The *Z* factor, a statistical parameter used for the validation and evaluation of the quality of a high-throughput screening (HTS) assay,[32] was calculated for this screening assay using the inhibitor mersalyl acid (MA), a thiophilic mercurial compound capable of inhibiting cysteine proteases, at 0.1 mM in the procedure described above. The mean and standard deviations of percent inhibition calculated for MA (positive inhibition control) and the vehicle control were then used to calculate the *Z* factor using eq 2:

$$Z\ \text{factor} = 1 - \frac{3(\sigma_I + \sigma_V)}{|\mu_I - \mu_V|} \quad (2)$$

where σ is the standard deviation, μ is the mean, I is the inhibition control, and V is the vehicle.

Steady-State Kinetics. Michaelis−Menten kinetics of purified N63 → Q mutant *Sa*Prp measured by cleavage of our FITC-conjugated peptide substrate were determined as previously described.[11] Measurements were taken in stabilizing buffer [50 mM $NaPO_4$ buffer (pH 7) containing 1.5 mM DTT, 2.35 mM EDTA, and 0.01% Tween 20] at ambient temperature. The Prp concentration was constant at 42.8 nM (calculated as a monomer), while the substrate concentration ranged from 0 to 20 μM. Fluorescence was tracked for 10 min [λ_{ex} = 488 nm (15 nm), and λ_{em} = 530 nm (15 nm); gain of 1500] to obtain initial velocities for each concentration.

Assay data were analyzed using Microsoft Excel for Microsoft 365 and GraphPad PrismVR (GraphPad, La Jolla, CA). Raw data were collected and organized in Excel. These data were then blank-corrected by subtracting the non-Prp-containing blank from the corresponding time points for each trial. The blank-corrected RFU data were then converted to cleaved substrate concentration using the equation of the standard curve (Figure S1) and plotted on a scatter plot. The slope of each curve's initial linear portion (initial velocity of approximately 0.5−3 min) was determined for each trial. The initial velocities for each substrate concentration were copied into Prism, where the data were analyzed using nonlinear regression fits to the Michaelis−Menten and k_{cat} equations (ET constrained to 42.8 nM active sites).

Fluorescence Interference Assay. Compounds were screened in a secondary fluorescence interference assay to assess the possible artifactual contribution to or subtraction from the measured fluorescence. A solution containing 1 μM FITC-conjugated peptide substrate and 21.4 nM *Sa*Prp (calculated as a dimer) was diluted to a final volume of 5 μL with the same assay buffer as in the fluorogenic cleavage assay. The fluorescence was determined after a 30 min incubation [λ_{ex} = 488 nm (15 nm), and λ_{em} = 530 nm (15 nm)]. The compounds were then added to the samples in triplicate to a final volume of 10 μM and incubated for 10 min while being shaken before the fluorescence reading was again obtained. Assay data were analyzed using Microsoft Excel for Microsoft 365. The relative percent change in fluorescence was calculated by eq 3:

https://doi.org/10.1021/acs.biochem.2c00010
Biochemistry 2022, 61, 1323−1336

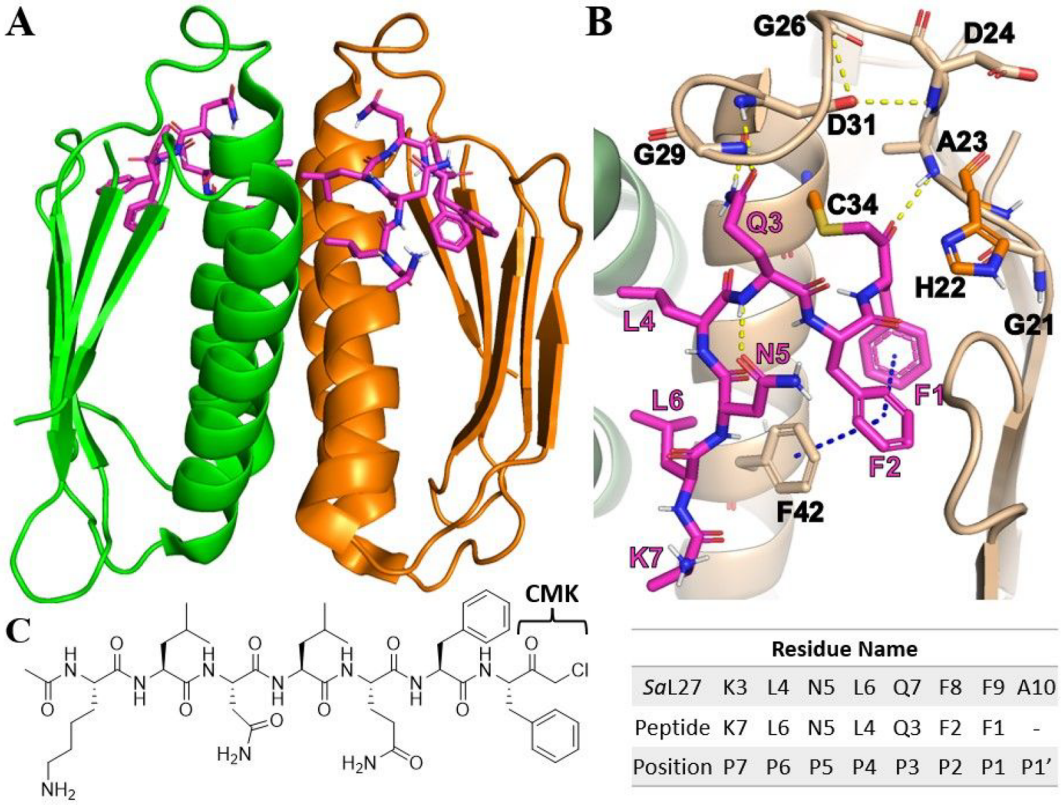

Figure 2. Crystal structure of Ac-KLNLQFF-CH_2- covalently bound to *Sa*Prp (PDB entry 7KLD). (A) Ribbon backbone of the *Sa*Prp noncrystallographic homodimer (orange and green subunits) showing the relative positions of the bound substrate/product Ac-KLNLQFF-CH_2- peptide (magenta). (B) Close-up of the substrate/product peptide (magenta) covalently bound as a thioether to Cys34 of chain B. Yellow and blue dashes depict hydrogen bonds and $\pi-\pi$ interactions, respectively. (C) Chemical structure of the Ac-KLNLQFF-CMK peptide inhibitor with the naming convention table. The polypeptide ligand numbering follows the convention of Schechter and Berger, beginning at the F1 cleavage site.[35]

$$\% \text{ change} = 100\left(\frac{X_f - X_i}{X_i}\right) \quad (3)$$

where X_f is the final fluorescence reading and X_i is the initial fluorescence reading.

Prp Stability. The activity of *Sa*Prp decreases over time in solution. We monitored this with our fluorogenic cleavage assay using 1 μM peptide substrate and three concentrations of *Sa*Prp (10.7, 21.4, and 42.8 nM calculated as monomer) over time with a freshly prepared solution from the purification stock (pH 8, 25 mM Tris, 10% glycerol) or stabilizing buffer [50 mM $NaPO_4$ buffer (pH 7), 1.5 mM DTT, 2.35 mM EDTA, and 0.01% Tween 20] stored at 4 °C. The initial velocity for each sample was calculated as described above and then plotted over time at different concentrations (Figure S2).

RESULTS

Crystal Structure of the SaPrp:Substrate Peptide Covalent Complex. Peptidyl-haloketones have been used as irreversible inhibitors of serine and cysteine proteases for many years. The peptidyl moiety, chosen to match the known specificity of the target enzyme, orients the inhibitor in the enzyme's active site such that the halomethylene group is juxtaposed to a catalytically functional nucleophile. In the case of cysteine proteases, such as papain, the methylene group of the haloketone reacts with the active site cysteine to form a covalent thioether bond with S_γ.[33] These substrates have also been used in the past to observe approximate substrate transition-state binding after a crystal structure has been elucidated.[34]

The previously available 4PEO *Sa*Prp crystal structure is missing a flexible segment, including the active site His22 catalytic residue. We hypothesized that the binding of a peptidyl-haloketone inhibitor with the *S. aureus* L27 N-terminal cleavage sequence (Ac-KLNLQFF-CMK) would stabilize the flexible chain segment of the unliganded *Sa*Prp. The inhibitor's productively bound configuration would lead to a nucleophilic attack of S_γ of Cys34 on the methylene group of the chloroketone to form a stable, covalent product-like complex. This approach was successful, leading to the first full-length *Sa*Prp structure that provides a detailed model of the interactions of *Sa*Prp with its substrate.

The crystal structure of the *Sa*Prp:Ac-KLNLQFF-CH_2- complex shows the active site Cys34 of both subunits of the biological homodimer covalently linked to the methylene group of the chloroketone suicide inhibitor (Figure 2A). The electron density of the peptide part of the inhibitor is complete except for the N-terminal acetyl-K residue, which is incomplete to different extents in the three noncrystallographic copies of the *Sa*Prp:peptide complex. The polypeptide segment that includes the functional His22 and is disordered in the unliganded *Sa*Prp structure (PDB entry 4PEO) is visible and interpretable in the electron density for the inhibitor complex.

In the absence of the bound substrate/product peptide, the disordered segment, hinged at residues Gly21 and Gly26, could adopt several positions in the 4PEO structure, including ones that intrude into the substrate/product binding site. This

https://doi.org/10.1021/acs.biochem.2c00010
Biochemistry 2022, 61, 1323−1336

would prevent the stable juxtaposition of the His22 imidazole side chain with a substrate and with the Cys34 nucleophilic side chain, which is required to assemble a functional active site of the enzyme. This implies that local conformational changes induced by binding of the substrate to *Sa*Prp are what confer activity on the initial Michaelis complex. This is confirmed by comparing the unliganded structures of the closely similar structures of *S. mutans* and *S. pneumoniae* (see below).

The thioether linkage of the covalently bound peptide heptamer inhibitor chain to S_γ of Cys34 differs in local conformation from a true substrate oxyanion thioester transition state (Figure 2B). True substrates of serine and cysteine proteases generally have two hydrogen bonds stabilizing the charge developed on the oxygen of this oxyanion. In the chloroketone inhibitor complex, the interposed ketone methylene group between S_γ of the active site Cys34 and the carbonyl of the proxy substrate scissile peptide bond displaces the keto oxygen from the oxyanion hole that a true substrate would occupy. In this covalent inhibitor structure, the carbonyl oxygen makes only a single hydrogen bond to the peptide backbone amide of Ala23 (2.8 Å). In the true substrate oxyanion transition state, the absence of the methylene group would result in rotational displacement of the oxyanion oxygen toward protonated $N_{\delta 1}$ of His22, which could undergo a slight side chain rotation to form the second stabilizing hydrogen bond of the transition state (Figure 2B).

The substrate polypeptide residues, numbered F1−K7 and corresponding to canonical residues P1−P7 (Figure 2C) from the scissile bond in Figure 2B, adopt a sinuous conformation with both intrapeptide and peptide−Prp hydrogen bonds as well as hydrophobic environments for F1, F2, L4, and L6. Residues F1−Q3 make the most extensive interactions with the *Sa*Prp, with the two phenylalanines buried in interior hydrophobic pockets. The Q3 side chain is also buried in an adjacent interior pocket, but with its side chain making a full complement of hydrogen bonds.

Comparison of the Structure of the SaPrp:Peptide Complex with Crystal Structures of Unliganded Prp. Two unliganded Prp crystal structures with ordered conformations of the chain corresponding to the Gly21−Gly26 segment in *Sa*Prp have been determined: *S. mutans* (PDB entry 2G0I) *Sm*Prp and *S. pneumoniae* (PDB entry 2IDL) *Sp*Prp. The sequences of both are moderately similar to that of *Sa*Prp, and when their structures are superimposed (Figure S3), there are virtually identical conformations over a large part of their C_α loci (for *S. mutans*, RMSD = 0.86 for 71 C_α atoms; for *S. pneumoniae*, RMSD = 0.70 for 63 C_α atoms). The *Sm*Prp conformation is not functional because of the intrusion of the mobile red segment into the binding site for the peptide substrate (magenta) and the dislocation of active site residue His22 (Figure 3). Displacement of this mobile segment coordinated with the binding of residues P1−P3 (F1-F2-Q3) of the substrate peptide and, we infer, of the absent downstream residues P1′−P3′ in this structure simultaneously positions His22 in a catalytically active state. The large blue arrows (Figure 3) show (1) the displacement of the red segment from the inactive *Sm*Prp conformation to the active *Sa*Prp conformation (yellow) and (2) the distal unwinding of almost one full turn of the terminus of the α-helix (red) to the coil conformation (yellow) that confers the mobility necessary for the adoption of the functional active site and the binding of the substrate.

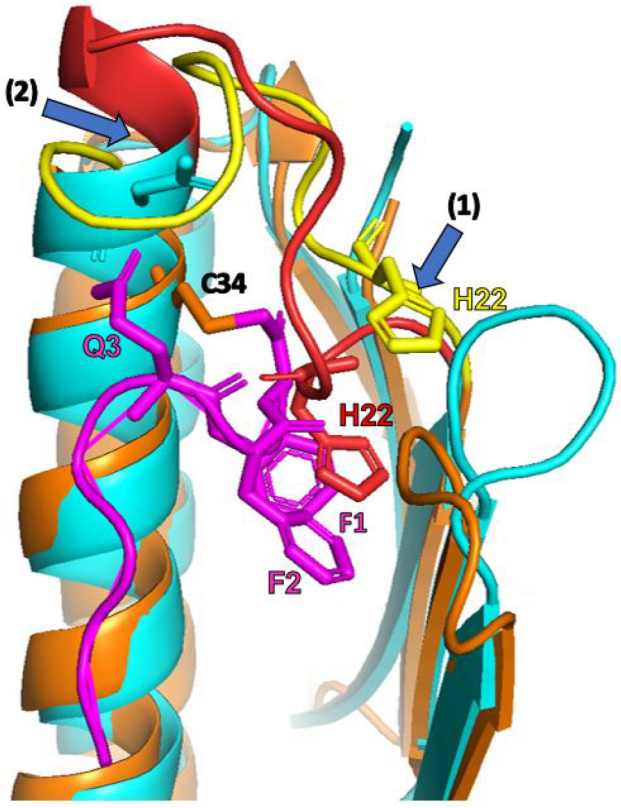

Figure 3. Alignment superposition of active site regions of *Sm*Prp (cyan and red, PDB entry 2G0I) and *Sa*Prp (orange and yellow, PDB entry 7KLD) bound to the peptide substrate (magenta). Blue arrows indicate significant changes in conformation between the structures.

These observations support the inference that displacement of the Gly21−Gly26 chain from the inactive conformation of Prps is coordinated with the binding of residues P1−P3 of a specific substrate (or inhibitor). This binding is the major, but not the only, determinant of the specificity of Prps for their pre-L27 substrate and is synchronized with the assembly of the functional active site of the enzyme.

Optimization of the Fluorogenic Cleavage Assay. Previous Prp fluorogenic cleavage assay iterations used a peptide substrate with non-optimal excitation and emission wavelengths, large assay volumes, and hand pipetting for all of the liquid transfers. We improved upon this assay by using a FITC-conjugated peptide [**1** (Figure 1)] in place of the 2-aminobenzoic acid (Abz) used in previous publications. This change in fluorophore reduced the fluorescence interference by many test compounds seen in the Abz assay. The original concentration of 1 μM fluorogenic peptide substrate resulted in a signal above the upper limit of quantification, so a concentration of 0.5 μM was used for further screening. We calculated a *Z*-score using both fluorophores and found that the FITC-conjugated peptide gave a *Z*-score (0.67) that was slightly higher than that of the Abz fluorophore (0.61). We also used the Labcyte Echo550 acoustic liquid handler to perform all liquid transfers. This allowed us to reduce the total assay volume from 200 to 5 μL while maintaining a consistent *Z*-score. The reduction in volume has a twofold benefit: reduction of material used and increased screening speed.

To ensure our assay was comparable to its previous iterations, we performed a Michaelis−Menten steady-state kinetic assay to determine the enzymatic kinetics of our

https://doi.org/10.1021/acs.biochem.2c00010
Biochemistry 2022, 61, 1323−1336

improved assay. This assay was performed the day Prp was produced and purified to obtain the highest possible activity because our stability studies show that Prp has a sharp decrease in activity (~50%) within the first 24 h after purification (Figure S2) unless kept in stabilizing buffer (defined in Materials and Methods). Using 48.2 nM *Sa*Prp (calculated as a monomer) and 0.2−20 μM fluorogenic peptide [**1** (Figure 1)], we were able to determine the V_{max} (11 ± 4.0 nM/s) and K_m (3.4 ± 1.8 μM) of *Sa*Prp by plotting the initial velocities over the concentration range of the substrate (Figure 4). The

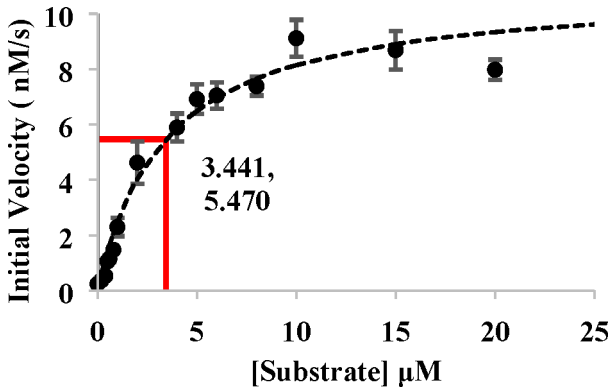

Figure 4. Michaelis−Menten plot of *Sa*Prp kinetics determined through cleavage of the FITC-KLNLQFFASKK-Dnp substrate. The average initial velocity is plotted vs the concentration of the fluorogenic peptide substrate. Data are means and standard deviations from experiments performed in triplicate.

catalytic turnover (k_{cat}) and catalytic efficiency (k_{cat}/K_m) were determined to be 0.26 ± 0.05 s^{-1} and 74,000 ± 38,000 M^{-1} s^{-1}, respectively. It is noteworthy that there appears to be a trend indicating that the FITC-conjugated peptide may be acting as an inhibitor at higher concentrations. This is consistent with *Sa*L27 peptide competition studies showing postcleavage products may act as partial competitive inhibitors.[11,17]

Chemical Inhibition of Prp. Mersalyl acid (**4**), an organomercurial that was historically used therapeutically as a diuretic,[36,37] was used in previous studies as a control for Prp inhibition, and we have continued its use here.[11] Mercury is thiophilic, so we hypothesize MA is targeting the active site cysteine in Prp as its mechanism of inhibition. This binding allows for potent inhibition of Prp but is unlikely to be selective in the presence of other cysteine-containing proteins. This lack of selectivity may be responsible for significant toxicity (including stomatitis, vertigo, thrombocytopenia, and/or severe hypotension) when MA is used therapeutically and was a significant contributing factor to the drug's withdrawal from the market by the Food and Drug Administration (FDA) in the 1960s.[38] While MA could arguably be placed into the category of "suicide inhibitor", its nonselectivity and toxicity remove it from consideration as a lead compound.

Compounds were screened at 100 μM using a FITC-conjugated peptide. Figure 5B compares positive and negative control conditions for the fluorogenic cleavage assay. As Prp cleaved the 11-mer peptide (KLNLQFFASKK), the quencher was released from the fluorophore, and fluorescence increased. When the MA (**4**) inhibitor was present, Prp could not cleave the peptide, and fluorescence did not increase. The *Z* factor (0.67) was calculated using these data based on percent

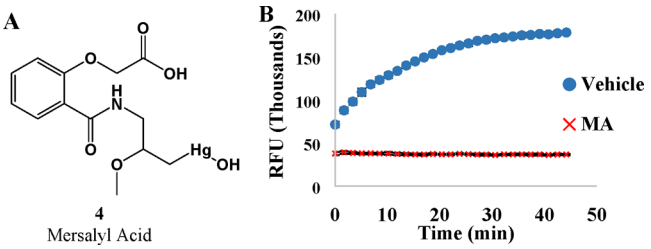

Figure 5. (A) Structure of mersalyl acid (**4**). (B) Change in the fluorescent signal over time. In the vehicle samples (blue), Prp cleaves the 11-mer conjugate, releasing the fluorophore. This process is inhibited in the mersalyl acid samples (red), and the 11-mer is not cleaved. Data are means and standard deviations from experiments performed in quintuplicate.

inhibition (eqs 1 and 2). MA was used as the positive inhibition control for all further studies.

We have screened a collection of 77 unique protease inhibitor compounds for their Prp inhibitory capacity. These were drawn from many compound classes, including peptidomimetics, nucleoside mimetics, dibenzazapines, macrolide-like types, and some containing an aromatic core (Chart S1). Many of these compounds are considered reversible inhibitors, often competitive or allosteric, such as those pictured in Figure 6A (**5**−**8**). There is also a subset that contains epoxides or aldehydes that covalently link to active site residues resulting in complete, irreversible inactivation of the protease [**9**−**14** (Figure 6A)]. A subset of these suicide inhibitors (**11**−**14**) are used in protease inhibitor cocktails due to their broad spectrum of inhibitory capability and to examine Prp's promiscuity.

An initial screen of the compounds was performed at 10 μM (Table S2) with no compounds exhibiting a percent inhibition of ≥50%. These compounds were also tested for fluorescence interference, and none had a percent change in fluorescence of ≥10%. We obtained the powder form of a collection of the compounds (**11**−**14**) that are irreversible cysteine protease inhibitors to screen at higher concentrations. We observed that none of these compounds has an IC_{50} of ≤100 μM (Figure 6B). Additionally, we observed that the Prp from *C. difficile* was unable to cleave the *Sa*L27-like substrate used in the *Sa*Prp assay (unpublished data), despite the close sequence similarity of the *S. aureus* and *C. difficile* pre-L27 proteins (Table 2). These results indicate *Sa*Prp has a highly evolved specificity for its endogenous substrate and resists inhibition by a broad range of commonly used protease inhibitors.

DISCUSSION

Crystal Structures of Prp. Knowledge of the three-dimensional molecular structure of an enzyme is now indispensable for drug design.[39] Such structures can be used for virtual screening and further refinement of drug candidates. In 2015, a high-resolution partial crystal structure (PDB entry 4PEO) for *Sa*Prp was published.[40] This publication antedated characterization and identification of the enzyme, but it was presumed to be associated with the ribosome due to the proximity of its gene to that of ribosomal protein L27. A significant drawback of this published structure is that the active site and catalytic residues from positions 22−34 are missing from the electron density, limiting its utility for drug design (Figure 7). This segment was presumed to be flexible, and we hypothesized that it is displaced and probably spatially

https://doi.org/10.1021/acs.biochem.2c00010
Biochemistry 2022, 61, 1323−1336

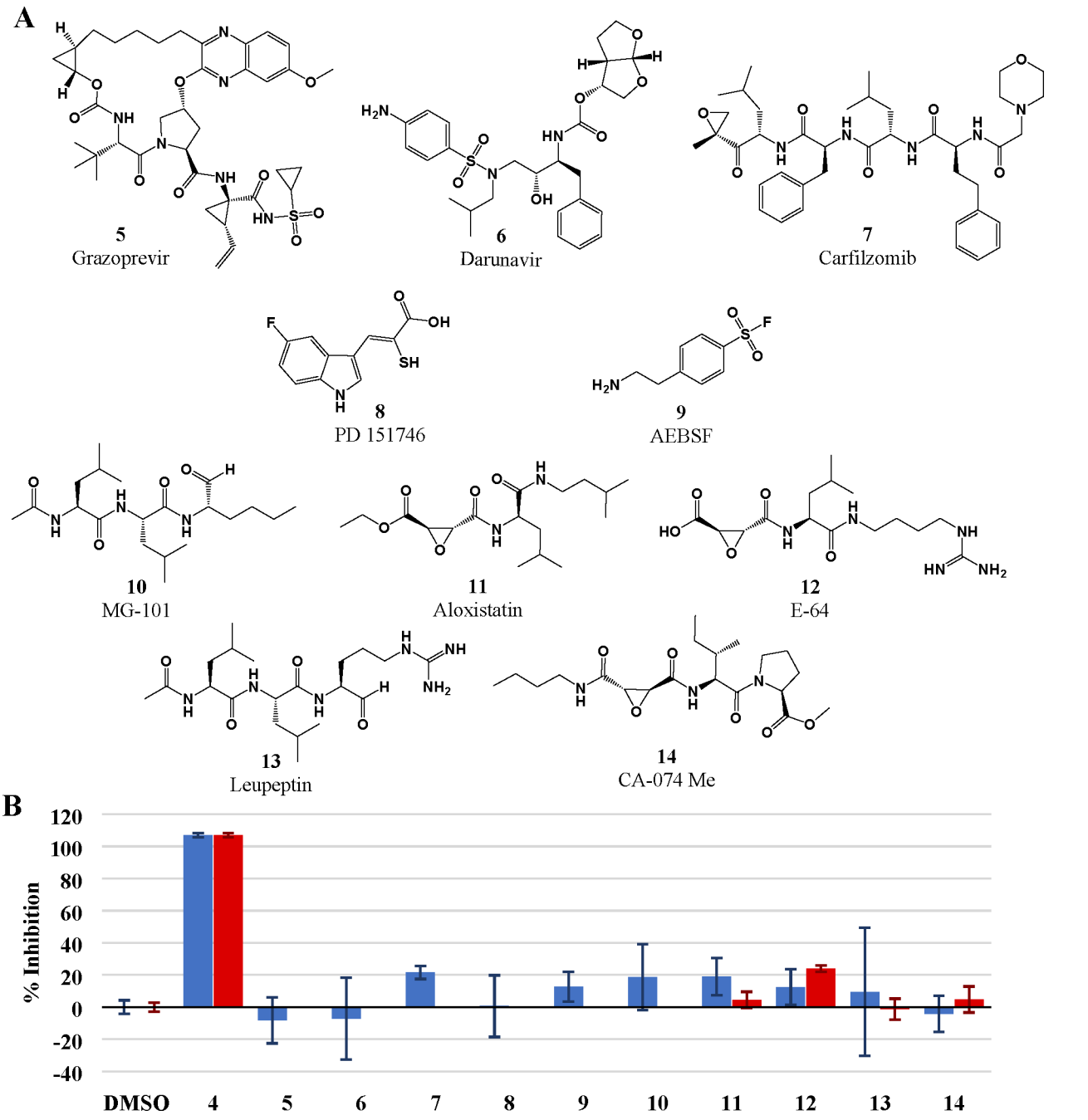

Figure 6. (A) Structures of a selection of the compounds analyzed for Prp inhibitory activity: grazoprevir (**5**), darunavir (**6**), carfilzomib (**7**), PD 151746 (**8**), 4-benzenesulfonyl fluoride hydrochloride (AEBSF, **9**), MG-101 (**10**), aloxistatin (**11**), E-64 (**12**), leupeptin (**13**), and CA-074 Me (**14**). Structures for all compounds screened are shown in Chart S1. (B) Percent inhibition data for compounds **4**–**14** at 10 μM (blue), including mersalyl acid (**4**) as the positive inhibition control, as well as the percent inhibition at 100 μM for the controls and cysteine protease suicide inhibitors (red). Data are means and standard deviations from experiments performed in triplicate.

stabilized upon binding the N-terminal pre-L27 sequence, thereby organizing the catalytic site and effecting cleavage.

To test this hypothesis, we designed a peptide substrate containing a chloroketone warhead capable of covalently binding to the catalytic cysteine of Prp (Cys34). Incubation of this peptide with *Sa*Prp gave >95% product with the expected molecular weight for a 1:1 complex as determined by mass spectrometry (Figure S4). Crystallization conditions, different from those used to obtain the 4PEO structure, were determined, and the crystals so obtained were used to obtain the structure described here. The crystal lattice of this covalent *Sa*Prp product complex consists of two types of Prp homodimers, one crystallographic and the other noncrystallographic (unit cell pictured in Figure S5). The noncrystallographic homodimer shows complete electron density for the main chain segment missing in the 4PEO model (Figure 7) and clear electron density for six or seven residues of the peptidyl group covalently bound as a thioether to Cys34 of *Sa*Prp. This new crystal structure will allow for the virtual screening and rational design of future inhibitors of *Sa*Prp.

The interactions of the product peptide with Prp are predominantly hydrophobic, beginning with the Phe-Phe

https://doi.org/10.1021/acs.biochem.2c00010
Biochemistry 2022, 61, 1323−1336

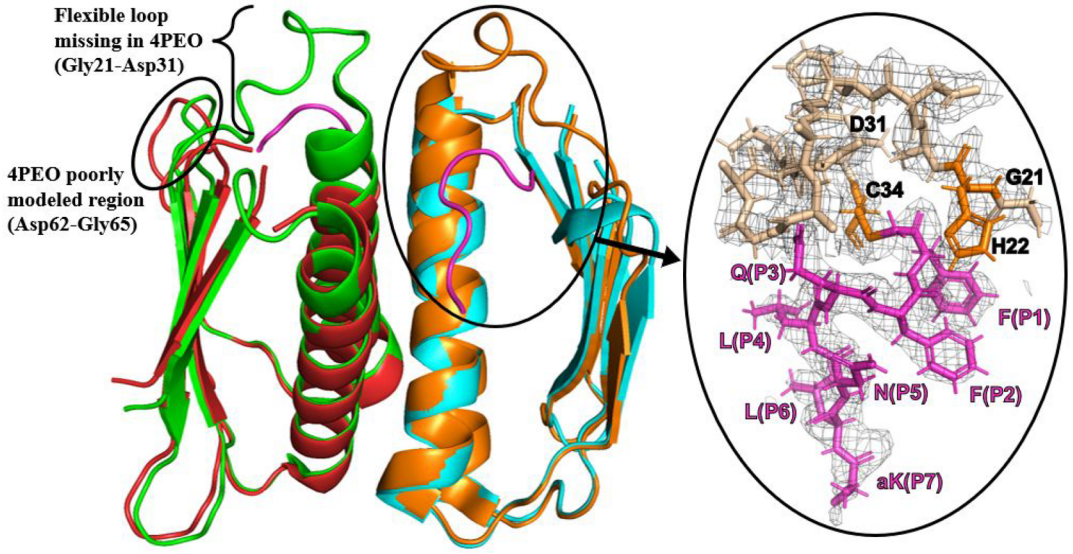

Figure 7. Covalent inhibitor substrate allows for complete resolution of catalytic flexible loop segment. Cartoon comparison of *Sa*Prp crystal structures (left). Unbound *Sa*Prp (red and cyan subunits, PDB entry 4PEO) overlaid with *Sa*Prp (green and orange subunits, PDB entry 7KLD) covalently bound to the Ac-KLNLQFF-CH_2- peptide (magenta). Electron density ($2mF_o - DF_c$ map) of the covalent substrate and flexible loop contoured at 1σ (right). Inhibitor peptide sequence binding subsites are indicated by cleavage position (P1−P7). The bronze Prp sequence shown is for the flexible region disordered in the unliganded structure (Gly21−Asp31) with catalytic residues (His22 and Cys34) colored orange. Substrate lysine side chain unresolved. Abbreviation: aK, acetyl-lysine.

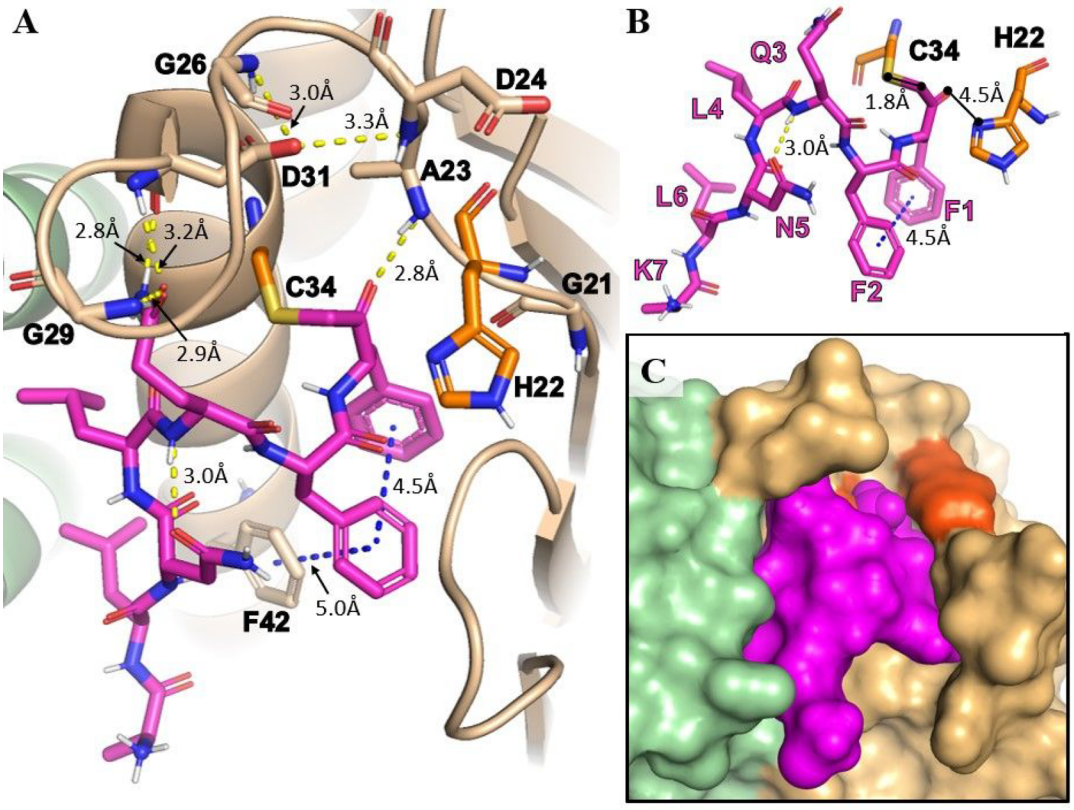

Figure 8. Interactions of Ac-KLNLQFF-CH_2- with the noncrystallographic homodimer of *Sa*Prp. (A) Inter- and intramolecular interactions between Prp chain B (bronze, His22 and Cys34 colored orange) and the peptide/substrate (magenta). Residues of Prp are labeled in bold. (B) View of substrate/product (magenta) in a bound conformation with catalytic residues (orange). (C) Space-filling model of the peptide substrate (magenta) bound to Prp (subunits colored bronze and light green). All images produced with PyMOL Molecular Graphics System, version 2.0 (Schrödinger, LLC).

sequence at positions P1 and P2 of the binding site and with the leucines at P4 and P6. The P1-P2 phenylalanines are buried in interior hydrophobic pockets and form a $\pi-\pi$ interaction network edge to face with Phe42 of Prp (Figure 8).

https://doi.org/10.1021/acs.biochem.2c00010
Biochemistry 2022, 61, 1323−1336

This network likely helps orient the peptide into the correct conformation for cleavage. Additionally, this structure reveals a significant size limitation at the P1′ position, which is occupied by alanine in native *S. aureus* pre-L27. This is supported by the sequence conservation of small residues (alanine, serine, etc.) in the P1′ and P2′ positions in other L27s (Tables 1 and 2).

The side chain of the P3 glutamine residue of the product/substrate peptide appears to play two critical roles: (i) It forms hydrogen bonds to Gly29 and Asp31 (Figure 8A) that stabilize one end of the mobile segment from Gly21 to Gly29 and thereby permits the juxtaposition of His22 to Cys34 for assembly of the catalytically active conformation, and (ii) it engages in an intrapeptide substrate hydrogen bond from its $N_{\varepsilon 2}$ to the peptide carbonyl oxygen of Leu at P4 (Figure 8B), which we hypothesize stabilizes the hydrolytically susceptible conformation of the peptide substrate. Coordinated with that stabilizing intrapeptide interaction is a similar hydrogen bond from the side chain amide oxygen of Asn at P5 of the peptide substrate to the peptide backbone nitrogen of Gln3. Together, these hydrogen bonds could help confer a preexisting stable conformation on the peptide substrate that is complementary to the Prp active site and may be an essential determinant of the high specificity of Prps. The significance of this residue is corroborated by the inability of *Sa*Prp to cleave the pre-L27 substrate in vitro when P3 is mutated to alanine or glutamic acid (unpublished data).

Our crystal structure also shows that half of a transition-state-stabilizing oxyanion hole is created by the peptide backbone amide of Ala23 in the flexible segment (Figure 8A). The other half of this oxyanion hole could be created by an $N_{\delta 1}$-protonated imidazole side chain of His22 following proton transfer from Cys34 during acyl-thioester intermediate formation or from solvent. The distance in the crystal structure from the thioester carbonyl oxygen to $N_{\delta 1}$ of His22 is 4.5 Å (Figure 8B), but in a true substrate missing the methylene group bound to S_γ of Cys34, the carbonyl oxygen would be slightly reoriented and with a slight rotation of the His22 imidazole side chain would be within hydrogen bonding distance of $N_{\delta 1}$ of the His22 imidazole.

Structural Analysis of Catalytically Inactive *Sa*Prp Mutants. The structure of unliganded *Sa*Prp,[21,40] in which a catalytic site chain segment is disordered, was earlier used by the Christie group to probe the roles of residues that were hypothesized to be functionally important in the absence of a catalytically competent *Sa*Prp crystal structure.[11] These mutants were almost entirely inactive (>97% loss of catalytic activity), consistent with their hypothesized essential functional roles.[11,41] However, the structure reported here permits a reinterpretation of the basis for the complete loss of enzymatic activity in several of these mutants.

G21A. This is the amino-terminal hinge point for reorientation of the labile segment extending to Gly29, the carboxyl-terminal hinge residue. These hinge glycines were inferred to be essential to the reorientation of the disordered catalytic polypeptide segment in the unliganded *Sa*Prp crystal structure to its ordered functional state. The presence of the G21A mutant on C_β of alanine at this position will hinder the main chain rotation required for reorientation, resulting in an inability to bind the substrate in a cleavable position.

H22A. Loss of activity in this mutant implies a functional role in catalysis and earlier was attributed to the loss of a critical proton acceptor group in the Cys34-His22 catalytic dyad. While it cannot be excluded as the proton acceptor from Cys34 with a rotation about X_1, the modeled extension of the substrate chain in the carboxyl direction from the thioester linkage implies that His22 would lie on the opposite side of the scissile bond and would be obstructed from accepting a proton from S_γ of Cys34. Its position in the peptidyl complex structure here makes it more likely to function as the general acid proton donor to the backbone amide leaving group on the carboxyl side of the scissile bond. The *Sa*Prp peptidyl complex determined here alters the earlier hypothesis that the His22 imidazole group functions as a proton acceptor from the active site Cys34 but instead indicates that it is transferring a proton to the leaving group product peptide.

D31A. Asp31 had previously been inferred to constitute part of a canonical Asp-His-Ser catalytic active site based on sequence conservation and the inactivity of the D31A mutant. This hypothesis, based partly on the mutant inactivity, is inconsistent with the structure described in this work. Instead, Asp31 appears to play a structural role in stabilizing the disordered chain that undergoes stabilization upon substrate binding, which is essential for catalytic competence. The aspartate side chain carboxylate in the wild type is sequestered between Cys34 and the β-turn loop His25−Cys34. This loop consists in part of residues that are reconfigured from the amino-terminal turn of the long α-helix (Ile32−Leu51). Asp31 stabilizes the loop through four hydrogen bonds to the main chain amide and also contributes a negative countercharge to the positive amino terminus of the reconfigured α-helix dipole. Some interaction between the Asp31 side chain and S_γ of Cys34 is possible but unlikely, and this conserved aspartate at Asp31 is clearly not part of a canonical charge relay system. Protonation of the Asp31 side chain from Cys34 would eliminate some of the loop-stabilizing interactions of Asp31 and be thermodynamically unfavorable and superfluous in that role. Asp31 appears to be primarily a structure-stabilizing group that, when lacking, eliminates activity through loss of local structure necessary for a functional catalytic active site.

C34S. The inactivity of this mutant is attributable to at least two related effects and should be considered in light of the H22A mutant, which constitutes the other half of a putative catalytic dyad. The pI of the mutant serine hydroxyl group is much higher than that of cysteine and requires a proton acceptor group to assist in the formation of the attacking seroxide nucleophilic group, as is the case in active serine proteases. At physiological pH, Cys34 is either deprotonated or readily activated by facile solvent deprotonation to the functional thiolate, obviating the requirement for the histidine proton acceptor. A modeled extension of the bound polypeptide toward the carboxyl terminus leaves the active site His22 imidazole side chain on the opposite side of the substrate and out of range for acceptance of a proton from a Ser34. It is possible but speculative that the larger sulfur on Cys34 will approach the imidazole close enough to transfer its proton, but the presence of the bound substrate seems likely to obstruct such a transfer (see the next section).

S38A. The S38A mutant retains a small residual activity (2.1 ± 0.2%), possibly reflecting its substrate affinity being slightly higher than those of other mutants. The crystal structure of the *Sa*Prp-peptidyl complex reveals a complex set of interactions of the serine side chain, which makes a 2.6 Å hydrogen bond to the carbonyl oxygen of Cys34 and long hydrogen bonds (3.5 and 3.6 Å) to the substrate backbone amide of Phe-Phe at P1 and P2. These latter hydrogen bonds are likely to be shorter when complexed with the natural substrate than in the

https://doi.org/10.1021/acs.biochem.2c00010
Biochemistry 2022, 61, 1323−1336

Table 3. Comparison of the Kinetic Parameters of *Sa*Prp to Those of Various Cysteine Proteases[a]

	K_m (μM)	k_{cat} (s^{-1})	k_{cat}/K_m (M^{-1} s^{-1})
*Sa*Prp[b]	3.4 ± 1.8	0.26 ± 0.05	74,000 ± 38,000
TEV protease[44]	61.0 ± 10.0	0.16 ± 0.01	2620 ± 460
papain[45]	0.62 ± 0.09	0.0162 ± 0.000135	26,000[c]
cathepsin B[46]	2000 ± 400	0.3 ± 0.05	150[c]
μ-calpain[47]	20.54 ± 2.28	0.015 ± 0.002	730 ± 46

[a]Values represent means and standard deviations. Abbreviation: TEV, tobacco etch virus. [b]Data from this work. [c]Standard deviation not reported.

chloromethylketone inhibitor due to the insertion of the methylene group into the inhibitor. Ser38 appears to stabilize the Cys34 orientation and interacts through hydrogen bonds with the peptide linkage of the P1 and P2 substrate residues. Without these crucial interactions, Cys34 and P1 cannot interact with each other to allow cleavage. The S38A mutant phenotype implicates this residue as necessary to *Sa*Prp catalysis but without the crystal structure would be difficult to interpret on a structural basis.

Comments on *Sa*Prp Properties In Vitro. The fluorogenic cleavage assay used in this work was modified to improve upon fluorescence interference and reduce total assay volumes. To ensure that our FITC fluorophore and decreased volume modifications to the assay did not affect the reproducibility, we determined the *Z*-score and kinetic constants and compared them with those from the previous Abz fluorophore iteration of the assay. The *Z*-scores were closely similar, with a slight increase in the new iteration (0.61 and 0.67, respectively). This is likely due to the reduction in hand pipetting, which decreased error.

The Michaelis−Menten kinetic constants were significantly altered in this new iteration of the assay procedure from those previously reported.[11] V_{max} is 5.6-fold higher, consistent with an increase in the concentration of active Prp ($[E_o]$). Full activity of Prp had been previously assumed, which overestimated $[E_o]$ due to the rapid loss of activity in the enzyme sample. This overestimated $[E_o]$ also influenced the earlier value of K_m, as the plateau of the initial velocity in that work was seen at lower substrate concentrations whose range extended to only 2.0 μM. The fractional activity of the *Sa*Prp sample, unknown in the absence of an active site titration but less than 1.0 as previously assumed, is consistent with the increase in k_{cat} and K_m from the fit of the new curve for the substrate dependence of the reaction rate. We attribute this increased $[E_o]$, at least in part, to the decreased time between *Sa*Prp production and purification. The degree of *Sa*Prp's steep decline in catalytic activity after purification was previously unknown and therefore had not been considered in the kinetic analysis. Additionally, liquid handling equipment significantly reduced the time from substrate addition to fluorescent reading (<30 s). Together, these factors resulted in more accurate and precise kinetic constants for *Sa*Prp catalytic activity.

*Sa*Prp was found to lose activity rapidly in the absence of DTT (Figure S2A), suggesting that its single cysteine residue, which is the active site nucleophile, is easily oxidized. The low pI (4.45) of *Sa*Prp may contribute to its susceptibility to oxidation.[42,43] The other two unliganded Prp structures (PDB entries 2G0I and 2IDL) do not appear to be oxidized at their active site cysteines, so it is unlikely that this oxidation is responsible for the lability of the chain beginning at residue 21. We made our activity measurements to determine kinetic constants during the first 24 h after purification of *Sa*Prp and in the presence of stabilizing assay buffer containing DTT to avoid loss of activity.

It has been hypothesized that Prp acts as a chaperone for L27 and a processing enzyme.[11] Known ribosomal protein chaperones share some characteristics with Prp, such as binding to the ribosomal protein's N-terminus during translation and genetic encoding directly upstream of the binding partner.[14] The high catalytic efficiency of *Sa*Prp relative to other cysteine proteases (Table 3) is partly due to its low K_m, and this, in turn, may reflect a slow k_{off} for the bound substrate or product of the *Sa*Prp-catalyzed reaction. This tight binding may facilitate a chaperone function for *Sa*Prp during ribosome maturation and may also serve to protect the active site cysteine from oxidation.

***Sa*Prp is a Highly Selective Protease.** The library of compounds screened with the fluorogenic cleavage assay includes a broad selection of protease inhibitors (Figure 6). We covered both large and small molecules and inhibitors of aspartic, serine, and cysteine proteases with various mechanisms of action (Table 4). Many of them are approved by the FDA for treating infectious diseases, such as hepatitis C and HIV, or genetic disorders, such as multiple myeloma. As shown in Figure 6B, all of these compounds have IC_{50} values of greater than 10 μM. Although this result is not unexpected for many of these compounds, such as **5**−**7**, it was surprising to discover that none of the protease inhibitors broadly targeting cysteine proteases (e.g., **10**−**14**) were inhibitory. This

Table 4. Targets and Binding Modes of Select Protease Inhibitors

	compound	binding	target
5	grazoprevir[48]	competitive	FDA-approved hepatitis C virus NS3/4A protease inhibitor
6	darunavir[49]	competitive	FDA-approved HIV-1 protease inhibitor
7	carfilzomib[50]	competitive	FDA-approved multiple myeloma treatment via proteasome inhibition
8	PD 151746[51]	allosteric	selective, cell-permeable calpain inhibitor with a K_i of 0.26 μM for μ-calpain
9	AEBSF[52]	irreversible	water-soluble, broad-spectrum serine protease inhibitor
10	MG-101[53]	irreversible	broad-spectrum, potent inhibitor of proteases, including lysosomal cathepsins and calpains
11	aloxistatin[54]	irreversible	membrane-permeable, broad-spectrum cysteine protease inhibitor that inhibits blood platelet aggregation
12	E-64[55]	irreversible	cysteine protease inhibitor that serves as the prototypical compound for epoxysuccinate protease inhibitors
13	leupeptin[56,57]	irreversible	broad-spectrum serine and cysteine protease inhibitor isolated from Actinomycetes
14	CA-074Me[58]	irreversible	cell membrane-permeable cathepsin B inhibitor

https://doi.org/10.1021/acs.biochem.2c00010
Biochemistry 2022, 61, 1323−1336

prompted us to perform a more selective screen at higher concentrations,

We screened peptidomimetics or peptide sequences with terminal aldehydes or epoxides, which can conjugate to an active site amino acid of a protease on binding to its active site, thereby rendering the protease incapable of turnover. These compounds are often used in broad-spectrum protease inhibitor cocktails that are used to protect assay components from endogenous proteases in cellular assays.[59] Compounds **11**−**14** were selected as examples due to their specificity for cysteine protease targets, their covalent, irreversible inhibitory mechanism, and their peptidic properties. It is noteworthy that a derivative of **12**, E-64d, has previously been shown to inhibit the peptide motif-directed cysteine protease in Chikungunya virus, called nsP2pro, which also uses a flexible loop to restrict access to the binding site.[60] Despite these predispositions as cysteine protease inhibitors, none of the compounds was capable of inhibiting Prp at 100 μM, indicating *Sa*Prp is resistant to traditional protease inhibitors.

CONCLUSIONS

These indications of a high level of substrate specificity for *Sa*Prp could be advantageous if an effective inhibitor can be developed. Any compound that can treat bacterial infections by specific inhibition of Prp should have a limited effect on commensal bacteria. Maintaining a thriving environment for commensal bacteria during antibiotic treatment would protect patients from secondary infections (e.g., *C. difficile*). Of the more than 40 officially recognized bacterial phyla, just six (Firmicutes, Fusobacteria, Synergistetes, Spirochetes, Tenericutes, and Thermotogae) have been shown to encode Prp. Only bacteria encoding long L27 should require Prp for ribosomal maturation, so the cytotoxic effects of inhibiting Prp should be limited to a relatively small spectrum of organisms, including pathogens *C. difficile*, *S. aureus*, and *S. pneumoniae*. In addition, the apparent exceptionally high resistance to traditional inhibitors by *Sa*Prp should confer a very narrow target window on effective Prp inhibitors. This limited spectrum of susceptible bacteria could attenuate the development of resistance by decreasing the selective pressure typically induced by broad-spectrum antibiotics.

Prp is the prototypical member of a new structural family of proteases (C.108) with no human homologues or previously published small-molecule inhibitors. We rationally designed a chloroketone peptide substrate inhibitor to inhibit *Sa*Prp irreversibly. This enzyme-inhibitor complex stabilized the flexible chain segment constituting part of the catalytic active site, allowing for the first fully resolved *Sa*Prp crystal structure. Additionally, it is the first Prp crystal structure of any phyla in a catalytically active conformation. The kinetic and stability characterization of Prp in this paper further defines Prp as a promising antibiotic target. The substrate specificity and resistance of Prp to conventional protease inhibitors indicate the potential for highly selective antibiotics and emphasize the need for rational drug design. The X-ray crystal structure and substrate specificity data described here provide valuable insights into key interactions necessary for Prp binding. Our results will assist and enable research on the discovery and design of compounds capable of inhibiting Prp.

ASSOCIATED CONTENT

Supporting Information

The Supporting Information is available free of charge at https://pubs.acs.org/doi/10.1021/acs.biochem.2c00010.

Table of crystallographic data and model refinement criteria (Table S1), a standard curve for the fluorogenic cleavage peptide (Figure S1), figures depicting *Sa*Prp stability (Figure S2), superimposition figures of known Firmicute Prp crystal structures (Figure S3), a chart and table of the protease inhibitors screened (Chart S1 and Table S2, respectively), mass spectrometric data for the *Sa*Prp:Ac-KLNLQFF-CH_2- complex after reaction (Figure S4), and the asymmetric unit of the *Sa*Prp:Ac-KLNLQFF-CH_2- complex crystal (Figure S5) (PDF)

Accession Codes

Proteins used in alignments: gp46, A4ZFB2; gp47, A4ZBF3; *Sa*L27, Q2FXT0; *Ec*L27, P0A7L8; *Bs*L27, P05657; *Cd*L27, Q18B22; *Ef*L27, A0A132ZFM0; *Lr*L27, K8QHR9; *Sm*L27, Q8DUQ4; *Sp*L27, P66136; *Fn*L27, Q8REI3; *Ac*L27, D5EEJ4; *Bb*L27, O51721; *Mp*L27, P47476; *Tm*L27, Q9X1G7. PDB entries: covalently bound *Sa*Prp, 7KLD; unliganded *Sa*Prp, 4PEO; *Sm*Prp, 2G0I; *Sp*Prp, 2IDL; *Tm*Prp, 1S1L.

AUTHOR INFORMATION

Corresponding Author

Aaron E. May − *Department of Medicinal Chemistry and Institute for Structural Biology, Drug Discovery and Development, Virginia Commonwealth University, Richmond, Virginia 23298, United States;* orcid.org/0000-0001-5314-9763; Email: aemay@vcu.edu

Authors

Julia A. Hotinger − *Department of Medicinal Chemistry and Institute for Structural Biology, Drug Discovery and Development, Virginia Commonwealth University, Richmond, Virginia 23298, United States*

Heather A. Pendergrass − *Department of Medicinal Chemistry and Institute for Structural Biology, Drug Discovery and Development, Virginia Commonwealth University, Richmond, Virginia 23298, United States*

Darrell Peterson − *Department of Medicinal Chemistry and Institute for Structural Biology, Drug Discovery and Development, Virginia Commonwealth University, Richmond, Virginia 23298, United States*

H. Tonie Wright − *Department of Medicinal Chemistry and Institute for Structural Biology, Drug Discovery and Development, Virginia Commonwealth University, Richmond, Virginia 23298, United States*

Complete contact information is available at: https://pubs.acs.org/10.1021/acs.biochem.2c00010

Author Contributions

A.E.M. and H.T.W. led and oversaw the studies. J.A.H., H.A.P., D.P., and H.T.W. conducted the experiments.

Funding

This research was funded by startup funds from the School of Pharmacy at Virginia Commonwealth University (VCU) and the 2021 VCU Presidential Research Quest Award Fund (PeRQ).

Notes

The authors declare no competing financial interest.

■ ACKNOWLEDGMENTS

The authors thank Gail Christie and Erin Wall for their foundational development of this project and continuing interest in the work.

■ ABBREVIATIONS

Abz, 2-aminobenzoic acid; AEBSF, 4-(2-aminoethyl)-benzenesulfonyl fluoride hydrochloride; CDC, Centers for Disease Control and Prevention; CMK, chloromethyl ketone; Dnp, dinitrophenyl; DMSO, dimethyl sulfoxide; DTT, dithiothreitol; EDTA, ethylenediaminetetraacetic acid; FDA, Federal Drug Administration; FITC, fluorescein isothiocyanate; HEPES, 4-(2-hydroxyethyl)-1-piperazineethanesulfonic acid; MA, mersalyl acid; MRSA, methicillin-resistant *S. aureus*; pI, isoelectric point; Prp, phage-related ribosomal protease; RMSD, root-mean-square deviation; *Sa*Prp, *S. aureus* Prp; SDS−PAGE, sodium dodecyl sulfate−polyacrylamide gel electrophoresis; *Sm*Prp, *S. mutans* Prp; *Sp*Prp, *S. pneumoniae* Prp; SUMO, small ubiquitin-like modifier; TCEP, tris(2-carboxyethyl)phosphine; TED, tris(carboxymethyl)-ethylenediamine; TEV, tobacco etch virus.

■ REFERENCES

(1) Talbot, G. H.; Jezek, A.; Murray, B. E.; Jones, R. N.; Ebright, R. H.; Nau, G. J.; Rodvold, K. A.; Newland, J. G.; Boucher, H. W. The Infectious Diseases Society of America's 10 × '20 Initiative (10 New Systemic Antibacterial Agents US Food and Drug Administration Approved by 2020): Is 20 × '20 a Possibility? *Clin. Infect. Dis.* **2019**, *69* (1), 1−11.

(2) Antibiotic Resistance Threats in the United States, 2019. Centers for Disease Control and Prevention: Atlanta, 2019.

(3) 2017 National and State Healthcare-Associated Infections Progress Report. Centers for Disease Control and Prevention: Atlanta, 2019.

(4) Gerber, J. S.; Ross, R. K.; Bryan, M.; Localio, A. R.; Szymczak, J. E.; Wasserman, R.; Barkman, D.; Odeniyi, F.; Conaboy, K.; Bell, L.; Zaoutis, T. E.; Fiks, A. G. Association of Broad- vs Narrow-Spectrum Antibiotics with Treatment Failure, Adverse Events, and Quality of Life in Children with Acute Respiratory Tract Infections. *JAMA* **2017**, *318* (23), 2325−2336.

(5) Melander, R. J.; Zurawski, D. V.; Melander, C. Narrow-Spectrum Antibacterial Agents. *Med. Chem. Comm.* **2018**, *9*, 12−21.

(6) Kolár, M.; Urbánek, K.; Látal, T. Antibiotic Selective Pressure and Development of Bacterial Resistance. *Int. J. Antimicrob. Agents* **2001**, *17* (5), 357−363.

(7) Abt, M. C.; Pamer, E. G. Commensal Bacteria Mediated Defenses against Pathogens. *Curr. Opin. Immunol.* **2014**, *29*, 16−22.

(8) Wall, E. A.; Caufield, J. H.; Lyons, C. E.; Manning, K. A.; Dokland, T.; Christie, G. E. Specific N-Terminal Cleavage of Ribosomal Protein L27 in *Staphylococcus aureus* and Related Bacteria. *Mol. Microbiol.* **2015**, *95* (2), 258−269.

(9) Spilman, M. S.; Damle, P. K.; Dearborn, A. D.; Rodenburg, C. M.; Chang, J. R.; Wall, E. A.; Christie, G. E.; Dokland, T. Assembly of Bacteriophage 80α Capsids in a *Staphylococcus aureus* Expression System. *Virology* **2012**, *434* (2012), 242−250.

(10) Trobro, S.; Åqvist, J. Role of Ribosomal Protein L27 in Peptidyl Transfer. *Biochemistry* **2008**, *47* (17), 4898−4906.

(11) Wall, E. A.; Johnson, A. L.; Peterson, D. L.; Christie, G. E. Structural Modeling and Functional Analysis of the Essential Ribosomal Processing Protease Prp from *Staphylococcus aureus*. *Mol. Microbiol.* **2017**, *104* (3), 520−532.

(12) Shin, D. H.; Lou, Y.; Jancarik, J.; Yokota, H.; Kim, R.; Kim, S. H. Crystal Structure of TM1457 from *Thermotoga maritima*. *J. Struct. Biol.* **2005**, *152* (2), 113−117.

(13) Rawlings, N. D.; Barrett, A. J.; Thomas, P. D.; Huang, X.; Bateman, A.; Finn, R. D. The MEROPS Database of Proteolytic Enzymes, Their Substrates and Inhibitors in 2017 and a Comparison with Peptidases in the PANTHER Database. *Nucleic Acids Res.* **2018**, *46*, D624−D632.

(14) Pillet, B.; Mitterer, V.; Kressler, D.; Pertschy, B. Hold on to Your Friends: Dedicated Chaperones of Ribosomal Proteins: Dedicated Chaperones Mediate the Safe Transfer of Ribosomal Proteins to Their Site of Pre-Ribosome Incorporation. *BioEssays* **2017**, *39* (1), e201600153.

(15) Chaudhuri, R. R.; Allen, A. G.; Owen, P. J.; Shalom, G.; Stone, K.; Harrison, M.; Burgis, T. A.; Lockyer, M.; Garcia-Lara, J.; Foster, S. J.; Pleasance, S. J.; Peters, S. E.; Maskell, D. J.; Charles, I. G. Comprehensive Identification of Essential *Staphylococcus aureus* Genes Using Transposon-Mediated Differential Hybridisation (TMDH). *BMC Genomics* **2009**, *10*, 291.

(16) Ji, Y.; Zhang, B.; Van Horn, S. F.; Warren, P.; Woodnutt, G.; Burnham, M. K. R.; Rosenberg, M. Identification of Critical Staphylococcal Genes Using Conditional Phenotypes Generated by Antisense RNA. *Science* **2001**, *293* (5538), 2266−2269.

(17) Wall, E. Elucidation of a Novel Pathway in *Staphylococcus aureus*: The Essential Site-Specific Processing of Ribosomal Protein L27. Virginia Commonwealth University, Richmond, VA, 2015.

(18) Yutin, N.; Puigbò, P.; Koonin, E. V.; Wolf, Y. I. Phylogenomics of Prokaryotic Ribosomal Proteins. *PLoS One* **2012**, *7* (5), No. e36972.

(19) Christis, G. E.; Damie, P.; Wall, E. A.; Dokland, T.; Poliakov, A. Target For Firmicutes and Related Bacteria the Prp Protease. U.S. Patent 2017/0049848A1, 2017.

(20) Oblessuc, P. R.; Matiolli, C. C.; Melotto, M. Novel Molecular Components Involved in Callose-Mediated Arabidopsis Defense against *Salmonella enterica* and *Escherichia coli* O157:H7. *BMC Plant Biol.* **2020**, *20*, 16.

(21) 4PEO: Crystal structure of a hypothetical protein from *Staphylococcus aureus*. https://www.rcsb.org/structure/4PEO (accessed 2021-05-28).

(22) 2IDL: Crystal Structure of Conserved Protein of Unknown Function from *Streptococcus pneumoniae*. https://www.rcsb.org/structure/2IDL (accessed 2021-05-28).

(23) Hou, H.-F.; Gao, Z.-Q.; Li, L.-F.; Liang, Y.-H.; Su, X.-D.; Dong, Y.-H. Crystal Structure of SMU.848 from *Streptococcus mutans*. *J. Chem. Inf. Model.* **2013**, *53* (9), 1689−1699.

(24) Evans, P. R. An Introduction to Data Reduction: Space-Group Determination, Scaling and Intensity Statistics. *Acta Crystallogr. Sect. D Biol. Crystallogr.* **2011**, *67* (4), 282−292.

(25) Evans, P. R.; Murshudov, G. N. How Good Are My Data and What Is the Resolution? *Acta Crystallogr. Sect. D Biol. Crystallogr.* **2013**, *69* (7), 1204−1214.

(26) Winn, M. D.; Ballard, C. C.; Cowtan, K. D.; Dodson, E. J.; Emsley, P.; Evans, P. R.; Keegan, R. M.; Krissinel, E. B.; Leslie, A. G. W.; Mccoy, A.; Mcnicholas, S. J.; Murshudov, G. N.; Pannu, N. S.; Potterton, E. A.; Powell, H. R.; Read, R. J.; Vagin, A.; Wilson, K. S. Overview of The CCP4 Suite and Current Developments. *Acta Crystallogr. Sect. D Biol. Crystallogr.* **2011**, *67* (4), 235−242.

(27) Mccoy, A. J.; Grosse-Kunstleve, R. W.; Adams, P. D.; Winn, M. D.; Storoni, L. C.; Read, R. J. Phaser crystallographic Software. *J. Appl. Crystallogr.* **2007**, *40* (4), 658−674.

(28) Liebschner, D.; Afonine, P. V.; Baker, M. L.; Bunkóczi, G.; Chen, V. B.; Croll, T. I.; Hintze, B.; Hung, L.-W.; Jain, S.; Mccoy, A. J.; Moriarty, N. W.; Oeffner, R. D.; Poon, B. K.; Prisant, M. G.; Read, R. J.; Richardson, J. S.; Richardson, D. C.; Sammito, M. D.; Sobolev, O. V.; Stockwell, D. H.; Terwilliger, T. C.; Urzhumtsev, A. G.; Videau, L. L.; Williams, C. J.; Adams, P. D. Macromolecular Structure Determination Using X-Rays, Neutrons and Electrons: Recent Developments in Phenix. *Acta Crystallogr. Sect. D Struct. Biol.* **2019**, *75* (10), 861−877.

(29) Afonine, P. V.; Grosse-Kunstleve, R. W.; Echols, N.; Headd, J. J.; Moriarty, N. W.; Mustyakimov, M.; Terwilliger, T. C.; Urzhumtsev, A.; Zwart, P. H.; Adams, P. D. Towards Automated Crystallographic Structure Refinement with *phenix.refine*. *Acta Crystallogr. Sect. D Biol. Crystallogr.* **2012**, *68* (4), 352−367.

https://doi.org/10.1021/acs.biochem.2c00010
Biochemistry 2022, 61, 1323−1336

(30) Emsley, P.; Lohkamp, B.; Scott, W. G.; Cowtan, K. Features and Development of Coot. *Acta Crystallogr. Sect. D Biol. Crystallogr.* **2010**, *66* (4), 486−501.
(31) Ernst, O.; Zor, T. Linearization of the Bradford Protein Assay. *J. Visualized Exp.* **2010**, *38*, 1918.
(32) Zhang, J. H.; Chung, T. D. Y.; Oldenburg, K. R. A Simple Statistical Parameter for Use in Evaluation and Validation of High Throughput Screening Assays. *J. Biomol. Screen.* **1999**, *4*, 67−73.
(33) Drenth, J.; Kalk, K. H.; Swen, M. Binding of Chloromethyl Ketone Substrate Analogues to Crystalline Papain. *Biochemistry* **1976**, *15* (17), 3731−3738.
(34) Schoellmann, G.; Shaw, E. Direct Evidence for the Presence of Histidine in the Active Center of Chymotrypsin. *Biochemistry* **1963**, *2* (2), 252−255.
(35) Schechter, I.; Berger, A. On the Size of the Active Site in Proteases. I. Papain. *Biochem. Biophys. Res. Commun.* **1967**, *27* (2), 157−162.
(36) Santos, K. L.; Vento, M. A.; Wright, J. W.; Speth, R. C. The Effects of Para-Chloromercuribenzoic Acid and Different Oxidative and Sulfhydryl Agents on a Novel, Non-AT1, Non-AT2 Angiotensin Binding Site Identified as Neurolysin. *Regul. Pept.* **2013**, *184*, 104−114.
(37) Kramer, M. J.; Cleeland, R.; Grunberg, E. Mersalyl: A Diuretic with Antiviral Properties. *Antimicrob. Agents Chemother.* **1975**, *8* (3), 295−299.
(38) Stewart, J. H.; Edwards, K. D. Clinical Comparison of Frusemide with Bendrofluazide, Mersalyl, and Ethacrynic Acid. *BMJ.* **1965**, *2* (5473), 1277−1281.
(39) Petsko, G. A.; Ringe, D. X-ray Crystallography in the Service of Structure-Based Drug Design. In *Drug Design: Structure- and Ligand-Based Approaches*; Merz, K. M., Jr., Ringe, D., Reynolds, C. H., Eds.; Cambridge University Press: Cambridge, U.K., 2010; pp 17−29.
(40) Chirgadze, Y. N.; Clarke, T. E.; Romanov, V.; Kisselman, G.; Wu-Brown, J.; Soloveychik, M.; Chan, T. S. Y.; Gordon, R. D.; Battaile, K. P.; Pai, E. F.; Chirgadze, N. Y. The Structure of SAV1646 from *Staphylococcus aureus* Belonging to a New' ribosome-Associated' Subfamily of Bacterial Proteins. *Acta Crystallogr. Sect. D Biol. Crystallogr.* **2015**, *71* (2), 332−337.
(41) Johnson, A. L. Characterization of a Novel Protease in *Staphylococcus aureus*. Virginia Commonwealth University, Richmond, VA, 2015.
(42) Sanchez, R.; Riddle, M.; Woo, J.; Momand, J. Prediction of Reversibly Oxidized Protein Cysteine Thiols Using Protein Structure Properties. *Protein Sci.* **2008**, *17* (3), 473−481.
(43) Bao, Y.; Boeren, S.; Ertbjerg, P. Myofibrillar Protein Oxidation Affects Filament Charges, Aggregation and Water-Holding. *Meat Sci.* **2018**, *135*, 102−108.
(44) Kapust, R. B.; Tözsér, J.; Fox, J. D.; Anderson, D. E.; Cherry, S.; Copeland, T. D.; Waugh, D. S. Tobacco Etch Virus Protease: Mechanism of Autolysis and Rational Design of Stable Mutants with Wild-Type Catalytic Proficiency. *Protein Eng. Des. Sel.* **2001**, *14* (12), 993−1000.
(45) Homaei, A. Enhanced Activity and Stability of Papain Immobilized on CNBr-Activated Sepharose. *Int. J. Biol. Macromol.* **2015**, *75*, 373−377.
(46) Brömme, D.; Bescherer, K.; Kirschke, H.; Fittkau, S. Enzyme-Substrate Interactions in the Hydrolysis of Peptides by Cathepsins B and H from Rat Liver. *Biochem. J.* **1987**, *245* (2), 381−385.
(47) Nguyen, H. H.; Varadi, M.; Tompa, P.; Pauwels, K. Affinity Purification of Human M-Calpain through an Intrinsically Disordered Inhibitor, Calpastatin. *PLoS One* **2017**, *12* (3), No. e0174125.
(48) Keating, G. M. Elbasvir/Grazoprevir: First Global Approval. *Drugs* **2016**, *76* (5), 617−624.
(49) Darwish, I. A.; Al-Majed, A. A.; Alsaif, N. A.; Bakheit, A. H.; Herqash, R. N.; Alzaid, A. Darunavir: A Comprehensive Profile. *Profiles Drug Subst., Excipients, Relat. Methodol.* **2021**, *46*, 1−50.
(50) Kortuem, K. M.; Stewart, A. K. Carfilzomib. *Blood* **2013**, *121* (6), 893−897.
(51) Siklos, M.; BenAissa, M.; Thatcher, G. R. J. Cysteine Proteases as Therapeutic Targets: Does Selectivity Matter? A Systematic Review of Calpain and Cathepsin Inhibitors. *Acta Pharm. Sin. B* **2015**, *5* (6), 506−519.
(52) Van Der Gucht, W.; Leemans, A.; De Schryver, M.; Heykers, A.; Caljon, G.; Maes, L.; Cos, P.; Delputte, P. L. Respiratory Syncytial Virus (RSV) Entry Is Inhibited by Serine Protease Inhibitor AEBSF When Present during an Early Stage of Infection. *Virol. J.* **2017**, *14* (1), 157.
(53) Zhang, S.; Shi, Y.; Jin, H.; Liu, Z.; Zhang, L.; Zhang, L. Covalent Complexes of Proteasome Model with Peptide Aldehyde Inhibitors MG132 and MG101: Docking and Molecular Dynamics Study. *J. Mol. Model.* **2009**, *15* (12), 1481−1490.
(54) Kundu, S. T.; Grzeskowiak, C. L.; Fradette, J. J.; Gibson, L. A.; Rodriguez, L. B.; Creighton, C. J.; Scott, K. L.; Gibbons, D. L. TMEM106B Drives Lung Cancer Metastasis by Inducing TFEB-Dependent Lysosome Synthesis and Secretion of Cathepsins. *Nat. Commun.* **2018**, *9* (1), 2731.
(55) Barrett, A. J.; Kembhavi, A. A.; Brown, M. A.; Kirschke, H.; Knight, C. G.; Tamai, M.; Hanada, K. L-Trans-Epoxysuccinyl-Leucylamido(4-Guanidino)Butane (E-64) and Its Analogues as Inhibitors of Cysteine Proteinases Including Cathepsins, B, H and L. *Biochem. J.* **1982**, *201* (1), 189−198.
(56) Aoyagi, T.; Miyata, S.; Nanbo, M.; Kojima, F.; Matsuzaki, M.; Ishizuka, M.; Takeuchi, T.; Umezawa, H. Biological Activities of Leupeptins. *J. Antibiot.* **1969**, *22* (11), 558−568.
(57) Desai, P. V.; Patny, A.; Gut, J.; Rosenthal, P. J.; Tekwani, B.; Srivastava, A.; Avery, M. Identification of Novel Parasitic Cysteine Protease Inhibitors by Use of Virtual Screening. 2. The Available Chemical Directory. *J. Med. Chem.* **2006**, *49* (5), 1576−1584.
(58) Patel, N.; Nizami, S.; Song, L.; Mikami, M.; Hsu, A.; Hickernell, T.; Chandhanayingyong, C.; Rho, S.; Compton, J. T.; Caldwell, J. M.; Kaiser, P. B.; Bai, H.; Lee, H. G.; Fischer, C. R.; Lee, F. Y. CA-074Me Compound Inhibits Osteoclastogenesis via Suppression of the NFATc1 and c-FOS Signaling Pathways. *J. Orthop. Res.* **2015**, *33* (10), 1474−1486.
(59) Wei, G.-X.; Bobek, L. A. Human Salivary Mucin MUC7 12-Mer-l and 12-Mer-d Peptides: Antifungal Activity in Saliva, Enhancement of Activity with Protease Inhibitor Cocktail or EDTA, and Cytotoxicity to Human Cells. *Antimicrob. Agents Chemother.* **2005**, *49* (6), 2336−2342.
(60) Narwal, M.; Singh, H.; Pratap, S.; Malik, A.; Kuhn, R. J.; Kumar, P.; Tomar, S. Crystal Structure of Chikungunya Virus NsP2 Cysteine Protease Reveals a Putative Flexible Loop Blocking its Active Site. *Int. J. Biol. Macromol.* **2018**, *116*, 451−462.

https://doi.org/10.1021/acs.biochem.2c00010
Biochemistry 2022, 61, 1323−1336